J Appl Electrochem (2011) 41:453–460
DOI 10.1007/s10800-011-0255-6

ORIGINAL PAPER

Improved high-rate cyclability of sol–gel derived Cr-doped spinel $LiCr_yMn_{2-y}O_4$ in an aqueous electrolyte

Wanmei Xu · Anbao Yuan · Lei Tian · Yuqin Wang

Received: 17 April 2010 / Accepted: 4 February 2011 / Published online: 19 February 2011

Abstract Spinel-type Cr-doped $LiCr_yMn_{2-y}O_4$ ($y = 0$, 0.1, 0.2) electrode materials were prepared via a sol–gel route starting with lithium acetate, manganese acetate and chromium nitrate as raw materials and citric acid as chelating agent. The phase structure and morphology of the materials were characterized by X-ray diffraction (XRD), transmission electron microscope (TEM) and scanning electron microscope (SEM) techniques. Electrochemical performances of the $LiCr_yMn_{2-y}O_4$ electrodes in 5 M $LiNO_3$ aqueous electrolyte were investigated using cyclic voltammetry, ac impedance and galvanostatic charge/discharge methods. Electrochemical results showed that Cr-doping could markedly improve the high-rate charge/discharge cyclability of the $LiMn_2O_4$ electrode in 5 M $LiNO_3$ aqueous solution.

Keywords Spinel $LiMn_2O_4$ · Cr-doping · Sol–gel method · Electrochemical performance · Cyclability · Aqueous electrolyte

1 Introduction

Spinel $LiMn_2O_4$ as positive electrode material for non-aqueous Li-ion batteries attracted great attentions in the past two decades owing to the advantages of abundant manganese resources, low cost and eco-friendly. In 1994, Dahn and co-workers [1] reported an aqueous Li-ion cell constructed with a $LiMn_2O_4$ positive electrode and 5 M $LiNO_3$ aqueous electrolyte. From that time on, aqueous Li-ion batteries attracted increasing interests in the world [2–6]. Aqueous Li-ion batteries own the merits of good safety, low cost and high specific power. In regard to the positive electrode materials for aqueous Li-ion batteries, spinel $LiMn_2O_4$ attracted the most interest [7–17]. It is well known that the stoichiometric spinel $LiMn_2O_4$ takes the cubic framework by close-stacked O^{2-} ions at the 32e sites [18], and can be simply expressed as $[Li]_{8a}[Mn^{4+}Mn^{3+}]_{16d}[O_4]_{32e}$. The Li^+ ions occupy the tetrahedral 8a sites, and the Mn^{4+} and Mn^{3+} ions locate at the octahedral 16d sites, with an average valence of 3.5 for Mn. When $LiMn_2O_4$ is charge/discharge cycled in the 4-V (vs. Li^+/Li) region, Li^+ ions deintercalate from and intercalate into $Li_xMn_2O_4$ over the x range $0 \leq x \leq 1$. However, when it is overdischarged at the 3-V level ($x > 1$), a structural transformation from cubic spinel phase ($LiMn_2O_4$) to tetragonal rock-salt phase ($Li_2Mn_2O_4$) will happen, i.e., the so called Jahn–Teller distortion, and results in a fast fading of capacity. Even if it is limited to charge and discharge only in the 4-V region, a capacity fading with the onset of Jahn–Teller distortion toward the end of the discharge in the cut-off limit between 4.2 and 3.4 V was observed [18]. Some research results demonstrated that doping of foreign metal cations less than tetravalent such as Al^{3+}, Co^{3+}, Cr^{3+} and Mg^{2+} etc. [19–22], partially replacing Mn, could increase the average valence of Mn in $LiMn_2O_4$ (decreasing the Mn^{3+} in $LiMn_2O_4$), and could depress the Jahn–Teller effect to a certain degree, and hence could improve the cyclability of $LiMn_2O_4$ in nonaqueous electrolytes. Although the electrochemical performances of doped $LiMn_2O_4$ in nonaqueous electrolytes have been studied intensively, the electrochemical study of doped $LiMn_2O_4$ in aqueous electrolytes is few. To the best of our knowledge, only two reports are available [12, 23]. One paper reported the structure variation of the Al-doped $LiAl_{0.15}Mn_{1.85}O_4$ upon

W. Xu · A. Yuan (✉) · L. Tian · Y. Wang
Department of Chemistry, College of Sciences, Shanghai University, Shanghai 200444, People's Republic of China
e-mail: abyuan@shu.edu.cn

charge/discharge in a $LiNO_3$ aqueous solution by in situ XRD method [23]; the other paper studied the cyclic voltammetric behaviors of the Cr-doped $LiCr_{0.15}Mn_{1.85}O_4$ electrode in a $LiNO_3$ aqueous solution [12]. However, the two papers did not report galvanostatic charge/discharge performance and cyclability of the doped $LiMn_2O_4$ in $LiNO_3$ solution.

In order to improve the cyclability of spinel $LiMn_2O_4$ in aqueous electrolyte, in the present study, the Cr-doped $LiCr_yMn_{2-y}O_4$ ($y = 0.1, 0.2$) spinels are prepared via a sol–gel route starting with lithium acetate, manganese acetate and chromium nitrate as raw materials and citric acid as chelating agent. The electrochemical performances of the Cr-doped $LiCr_yMn_{2-y}O_4$ electrodes in 5 M $LiNO_3$ aqueous solution were investigated and compared with those of the pristine $LiMn_2O_4$, especially, with respect to the long-term charge/discharge cyclability at a high current rate.

2 Experimental

2.1 Preparation of $LiCr_yMn_{2-y}O_4$ ($y = 0, 0.1, 0.2$) materials

Stoichiometric amounts of lithium acetate ($LiAc{\cdot}2H_2O$), manganese acetate ($Mn(Ac)_2{\cdot}4H_2O$) and chromium nitrate ($Cr(NO_3)_3{\cdot}9H_2O$) were dissolved in distilled water. In addition, required amount of citric acid ($C_6H_8O_7{\cdot}H_2O$, the molar ratio of citric acid to the total amount of metal ions is 1:1) was dissolved in distilled water. The two solutions were mixed and stirred with a magnetic stirrer. After stirring for 10 min, given amount of polyethylene glycol (PEG-200, 2.7 wt% of the total mass of the reactants including citric acid) was added dropwise to the solution (in favor of the gelation process afterwards and as a dispersant). Then, strong aqua ammonia was added to the solution drop by drop until pH $\approx$ 7. The solution was heated to 80 °C and then kept at this temperature for evaporation of water under stirring. With continuous evaporation, the solution became a semi-transparent sol with purple color, and finally, a concentrated gel was obtained. The gel was dried in a drying box at 105 °C for 4 h and ground to fine powders (precursor). The precursor was calcined in air in a muffle furnace at 700 °C for 12 h. After cooling, the $LiCr_yMn_{2-y}O_4$ material was obtained. In addition, in order to investigate the effect of calcination temperature on the structure and electrochemical performance of $LiMn_2O_4$, three pristine $LiMn_2O_4$ materials (without Cr doping) were also prepared by calcination at different temperatures (500, 600 and 700 °C, respectively) for 12 h using the same method and procedure.

2.2 Physical characterization of $LiCr_yMn_{2-y}O_4$ materials

X-ray diffraction (XRD) analysis of the $LiCr_yMn_{2-y}O_4$ materials was conducted on a Rigaku D/max-2000 X-ray powder diffractometer with a Cu K_α radiation (40 kV, 40 mA) over the 2θ range 10–90°. Morphological observation of the materials was carried out using a JEOL JEM-200CX transmission electron microscope (TEM) and a JSM-6700F field-emission scanning electron microscope (FE-SEM).

2.3 Fabrication and electrochemical testing of $LiCr_yMn_{2-y}O_4$ electrodes

$LiCr_yMn_{2-y}O_4$ electrodes were prepared as follows: $LiCr_yMn_{2-y}O_4$ active material, acetylene black (AB) conductor and polytetrafluoroethylene binder (PTFE emulsion) were mixed thoroughly to form slurry. The slurry was coated onto a titanium mesh current collector with an apparent area of 1 cm × 1 cm, dried at 80 °C for 12 h, and then roll-pressed to a sheet. The weight ratio $LiCr_yMn_{2-y}O_4$/AB/PTFE is 75:20:5.

Electrochemical measurements of the $LiCr_yMn_{2-y}O_4$ electrodes were performed in a glass cell with three-electrode configuration, using $LiCr_yMn_{2-y}O_4$ and activated carbon as the working and counter electrodes, respectively, and saturated calomel electrode (SCE) as the reference electrode, and 5 M $LiNO_3$ aqueous solution as the electrolyte. Cyclic voltammetry and ac impedance measurements were carried out using a Solartron instrument Model 1287 coupled with a 1255B FRA. Charge/discharge tests were conducted using a LAND 2001A auto-cycler (China). All the tests were conducted at 30 °C.

3 Results and discussion

3.1 Structure and morphology of $LiCr_yMn_{2-y}O_4$ materials

Figure 1a shows the XRD patterns of the pristine $LiMn_2O_4$ calcined at different temperatures (500, 600 and 700 °C) for 12 h. As can be seen, all the materials exhibit the characteristic diffraction peaks of the cubic spinel $LiMn_2O_4$ with *Fd3m* space group (PDF 35-0782). The peak intensity increases and the peak width decreases simultaneously with increasing calcination temperature, suggesting an increase in crystallinity. In addition, two weak diffraction peaks can be observed at ca. 32.5° and 55.5° for the samples calcined at 600 and 700 °C, which correspond to the two strongest characteristic diffraction peaks of Mn_2O_3 (PDF 78-0390), indicating the presence of trace

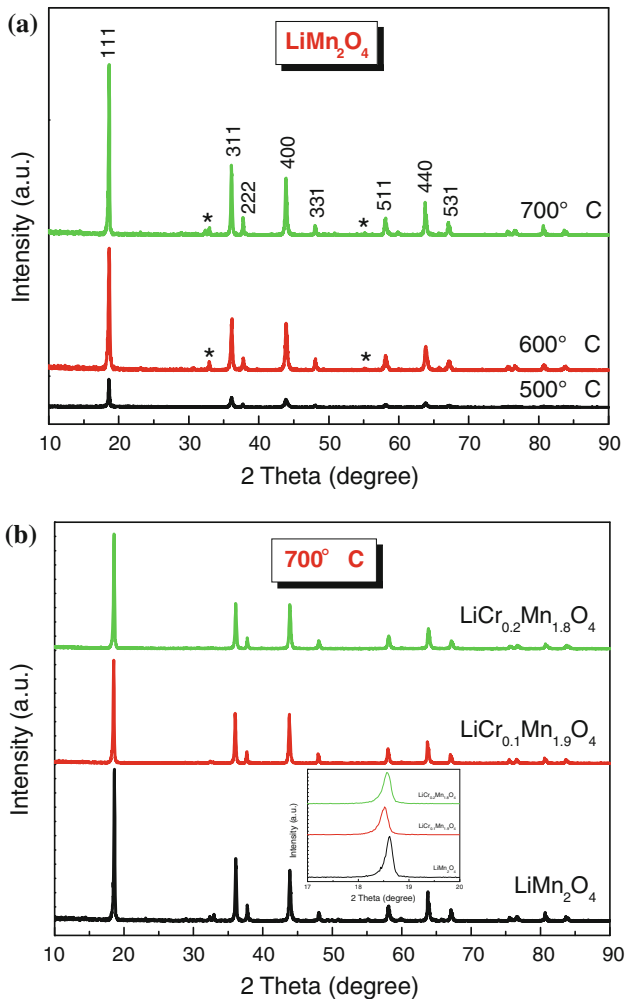

Fig. 1 XRD patterns of **a** pristine $LiMn_2O_4$ calcined at different temperatures, and **b** $LiCr_yMn_{2-y}O_4$ calcined at 700 °C

amount of Mn_2O_3 impurity phase in the materials. Figure 1b shows the XRD patterns of the Cr-doped $LiCr_yMn_{2-y}O_4$ ($y = 0.1, 0.2$) calcined at 700 °C for 12 h in comparison with that of the pristine $LiMn_2O_4$. In the case of the doped oxides only a reduced impurity peaks at ca. 32.5° can be observed in comparison with the pristine oxide. This suggests that presence of Cr can hinder the formation of Mn_2O_3 in the calcination process. In addition, It can be seen that compared with the pristine $LiMn_2O_4$, the diffraction peaks of the $LiCr_yMn_{2-y}O_4$ ($y = 0.1, 0.2$) are lowered and a little broadened (see the inset showing a detail of a selected (111) peak), suggesting a reduction of crystallinity with Cr-doping.

Table 1 lists the lattice parameters and cell volumes of the pristine $LiMn_2O_4$ calcined at different temperatures and the Cr-doped $LiCr_yMn_{2-y}O_4$ calcined at 700 °C. The lattice parameter and the cell volume of the pristine $LiMn_2O_4$ increase with increasing calcination temperature (especially, increasing from 600 to 700 °C). This result can be explained by the existence of cation vacancies at low temperature [24]. Compared with the $LiMn_2O_4$ calcined at 700 °C, the lattice parameter of the $LiCr_{0.1}Mn_{1.9}O_4$ is increased and that of the $LiCr_{0.2}Mn_{1.8}O_4$ is decreased. Generally, the lattice parameter of Cr-doped $LiMn_2O_4$ decreases with increasing Cr content and this would be explained as follows [25–27]: because the radius of Cr^{3+} is smaller than that of Mn^{3+}, and hence result in a structure contraction and a decreased lattice parameter. The increase in lattice parameter of the $LiCr_{0.1}Mn_{1.9}O_4$ in the present work is not clear at the present time. However, a similar phenomenon was also observed in the literature [28], where the lattice parameter of the LMO spinel does not decrease continuously with increasing Cr content.

Figure 2a and b show the TEM photographs of the pristine $LiMn_2O_4$ calcined at 600 and 700 °C, respectively, and Fig. 2c and d show the TEM photographs of the 700 °C calcined $LiCr_{0.1}Mn_{1.9}O_4$ and $LiCr_{0.2}Mn_{1.8}O_4$, respectively, and Fig. 2e and f show the SEM photographs of the 700 °C calcined $LiCr_{0.1}Mn_{1.9}O_4$ and $LiCr_{0.2}Mn_{1.8}O_4$, respectively. As can be seen, the $LiMn_2O_4$ material obtained at 600 °C consists of aggregates of irregular crystallites with different crystallite sizes generally less than 100 nm. While, the $LiMn_2O_4$ material obtained at 700 °C consists of aggregates of regular crystallites with an increased size of ca. 200 nm. The $LiCr_{0.1}Mn_{1.9}O_4$ and $LiCr_{0.2}Mn_{1.8}O_4$ materials obtained at 700 °C consist of aggregates of regular crystallites with different crystallite sizes generally ranging from ca. 100–300 nm. From these results we can see that calcination temperature and Cr-doping have important influence on the morphology and crystallinity of the spinels. The crystallinity increases with increasing calcination temperature, which is consistent with the XRD results. The decreased diffraction intensities observed in the XRD patterns for the

Table 1 Lattice parameters and cell volumes of pristine $LiMn_2O_4$ calcined at different temperatures and Cr-doped $LiCr_yMn_{2-y}O_4$ calcined at 700 °C

Sample	LMO (500 °C)	LMO (600 °C)	LMO (700 °C)	LMO ($y = 0.1$)	LMO ($y = 0.2$)
Lattice parameter (Å)	8.23648	8.23795	8.24734	8.25294	8.24075
ESD value	0.001823	0.001142	0.000584	0.001141	0.001137
Cell volume ($Å^3$)	558.76	559.06	560.97	562.12	559.63

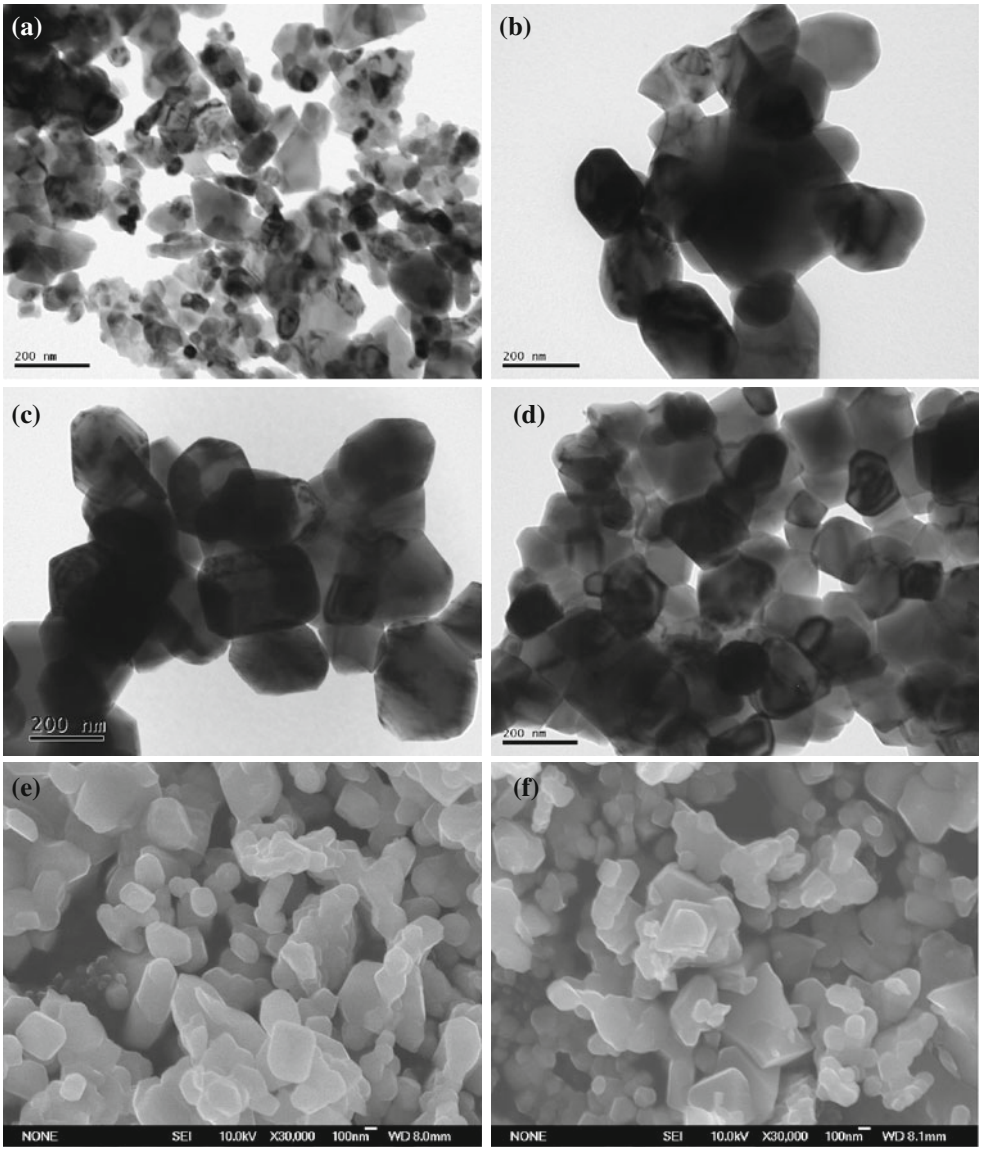

Fig. 2 TEM photographs of pristine $LiMn_2O_4$ calcined at **a** 600 °C and **b** 700 °C, and **c** $LiCr_{0.1}Mn_{1.9}O_4$ and **d** $LiCr_{0.2}Mn_{1.8}O_4$ calcined at 700 °C, and SEM photographs of **e** $LiCr_{0.1}Mn_{1.9}O_4$ and **f** $LiCr_{0.2}Mn_{1.8}O_4$ calcined at 700 °C

700 °C calcined Cr-doped spinels compared to that of the 700 °C calcined pristine $LiMn_2O_4$ may be related to their wider distribution of crystallite size.

3.2 Electrochemical performance

Figure 3a shows the cyclic voltammographs (CVs) of the pristine $LiMn_2O_4$ electrodes derived from calcination at different temperatures for 12 h at a scan rate of 1 mV s^{-1}. As can be seen, in the potential range of 0.2–1.4 V (vs. SCE), the $LiMn_2O_4$ electrodes exhibit two couples of reversible redox waves, which correspond to the intercalation and deintercalation of Li^+ ions together with exchange of electrons (redox of Mn^{4+}/Mn^{3+} in the spinel) [12, 17]. The redox current peaks of the 700 °C derived $LiMn_2O_4$ are higher than those of the 500 and 600 °C derived $LiMn_2O_4$, suggesting a higher electrochemical activity of the former. This may be related to the higher crystallinity of the 700 °C derived $LiMn_2O_4$. In addition, the charge/discharge cyclability of the 700 °C derived $LiMn_2O_4$ is also superior to that of the 500 or 600 °C derived $LiMn_2O_4$ (Fig. 3b). Hence, the Cr-doped $LiCr_yMn_{2-y}O_4$ materials are prepared with calcination at 700 °C. The electrochemical performances of the $LiCr_yMn_{2-y}O_4$ ($y = 0$, 0.1, 0.2) electrodes are compared and discussed afterwards.

The CVs of the 700 °C calcined $LiCr_{0.1}Mn_{1.9}O_4$ and $LiCr_{0.2}Mn_{1.8}O_4$ electrodes in comparison with that of the

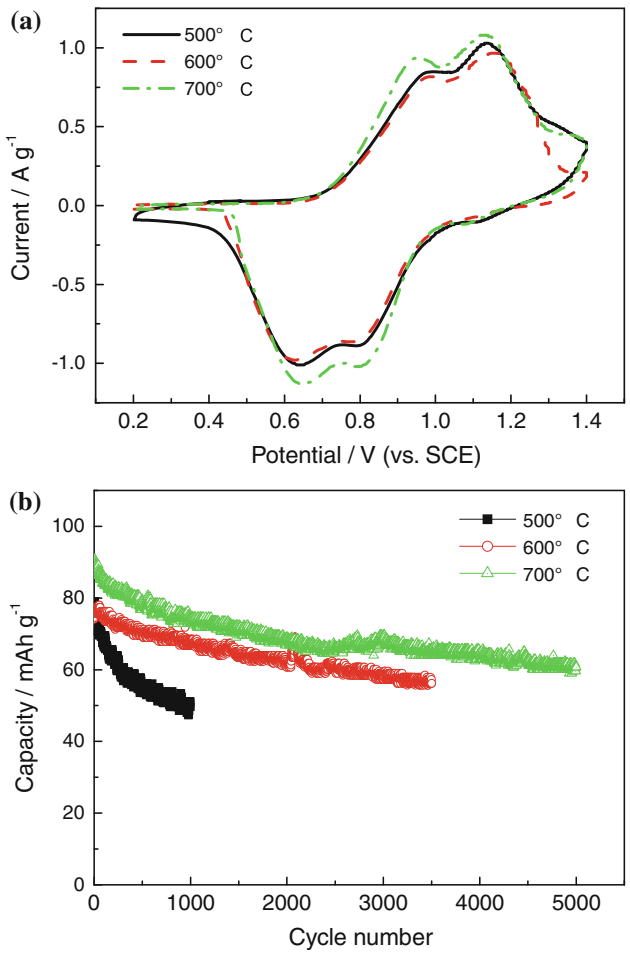

Fig. 3 Cyclic voltammographs (**a**) and cycle performances at 2,000 mA g^{-1} (**b**) of $LiMn_2O_4$ electrodes derived from calcination at different temperatures

pristine $LiMn_2O_4$ electrode at a scan rate of 1 mV s^{-1} are shown in Fig. 4. Compared with the $LiMn_2O_4$ electrode, the reduction current response and the corresponding encircled area for the $LiCr_{0.1}Mn_{1.9}O_4$ electrode are decreased a little, while the current peaks of Li^+ intercalation and deintercalation for the $LiCr_{0.2}Mn_{1.8}O_4$ electrode are decreased obviously, especially for the redox couple of the high-potential waves. Besides, an oxygen evolution current peak is observed in the potential range of ca. 1.25–1.4 V. In fact, constant-current charge/discharge results demonstrate that when the $LiCr_{0.2}Mn_{1.8}O_4$ electrode or other a lithium–manganese spinel electrode is charge/discharge cycled at a current rate lower than 500 mA g^{-1}, the charge/discharge current efficiency is indeed lower than 100% due to the oxygen evolution upon charging up to a higher potential. However, when the current rate is increased to 500 mA g^{-1} or higher, the current efficiency is increased close to 100%. The current-rate dependence of oxygen evolution should be due to the competition between Li^+ extraction and oxygen evolution, which are decided by the kinetics of the two reactions. In addition, we can see that the two couples of redox waves tend to fade away (becoming obscure or overlapped) as the Cr content increasing. This result is similar to the CV behaviors of the $LiCr_yMn_{2-y}O_4$ electrodes in a nonaqueous electrolyte [29].

Figure 5 shows the Nyquist plots of the $LiCr_yMn_{2-y}O_4$ electrodes measured over the frequency range of 10^5–10^{-2} Hz. The inset is the enlargement of the impedance data in high frequency region. The impedance data are calculated based on the mass of the $LiCr_yMn_{2-y}O_4$ active material and normalized in Ohm g for comparison. As can be seen, all the impedance plots consist of a high-frequency arc and a low-frequency line. The high-frequency arc should be ascribed to the charge transfer process relating to the charge transfer resistance, and the low-frequency line corresponds to the solid-phase diffusion process of Li^+ ions in $LiCr_yMn_{2-y}O_4$. With decreasing frequency, the

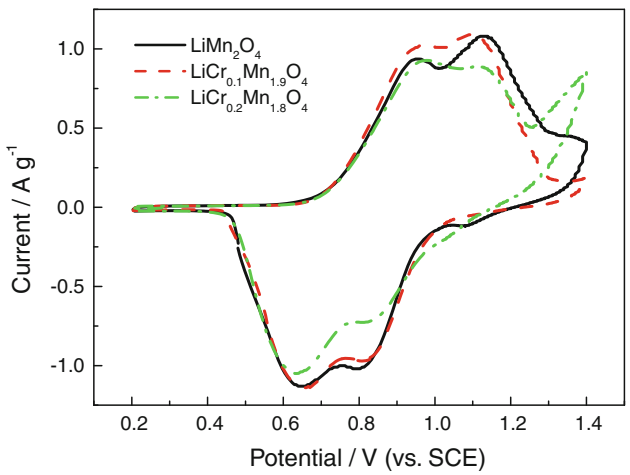

Fig. 4 Cyclic voltammographs of $LiCr_yMn_{2-y}O_4$ electrodes with different Cr contents

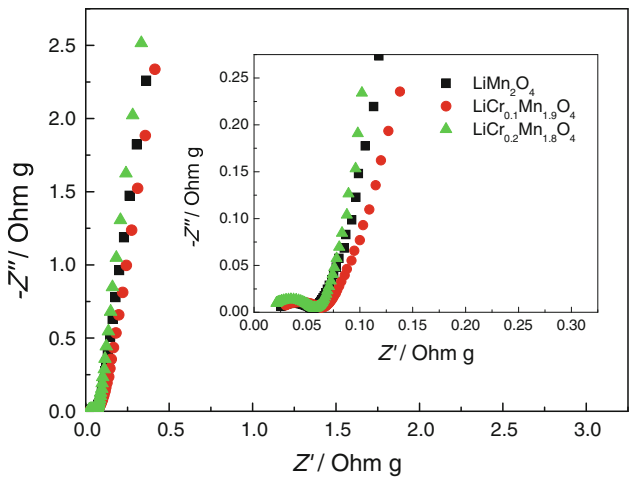

Fig. 5 Nyquist plots of $LiCr_yMn_{2-y}O_4$ electrodes with different Cr contents

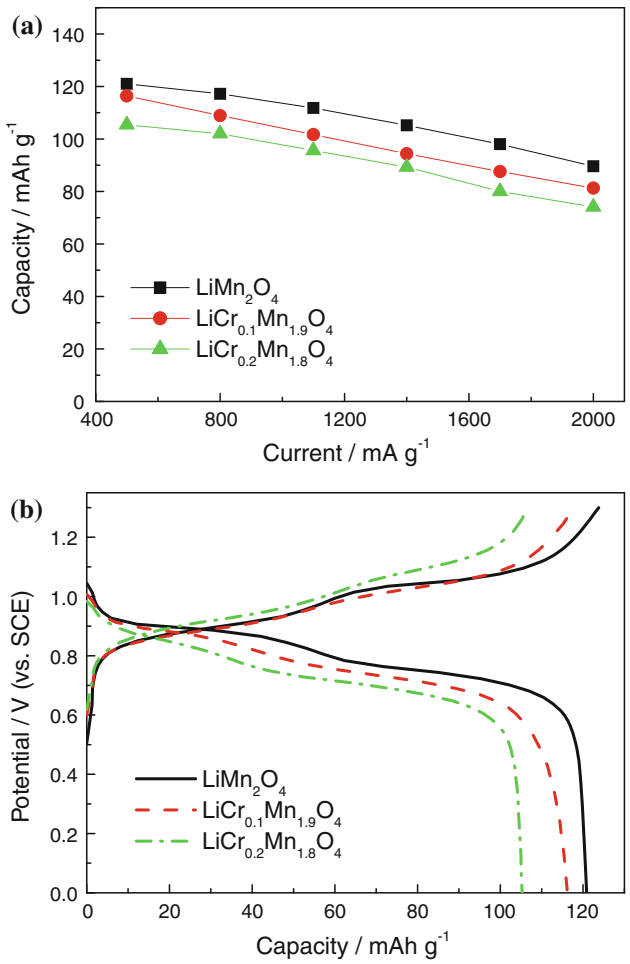

Fig. 6 Specific capacities at different current rates (**a**), and charge–discharge curves at 500 mA g^{-1} (**b**) of $LiCr_yMn_{2-y}O_4$ electrodes with different Cr contents

slope of the line increases gradually (larger than 45°), exhibiting a typical diffusion characteristic of a porous electrode, rather than an ideal Warburg semi-infinite diffusion [30]. Judging from the impedance plots, all the electrodes show approximately equal total impedance. The charge transfer resistances of the electrodes are relatively small compared to the diffusion impedances, which is different from $LiMn_2O_4$ spinel in nonaqueous solution [31]. In aqueous solution, the charge transfer process is relatively fast, and the electrode reaction kinetics is mainly controlled by the diffusion of Li^+ ions in solid.

Figure 6a shows the specific capacities of the $LiCr_yMn_{2-y}O_4$ electrodes at different charge/discharge current rates over the potential range of 0–1.3 V (SCE). The current rates and specific capacities are calculated based on the mass of the $LiCr_yMn_{2-y}O_4$ active material. As can be seen, in the current range of 500–2,000 mA g^{-1}, the specific capacities of the electrodes decrease with increasing current rate and follow the order of $LiMn_2O_4 > LiCr_{0.1}Mn_{1.9}O_4 > LiCr_{0.2}Mn_{1.8}O_4$ at any a current rate. That is to say, the specific capacity decreases with increasing Cr content. When the current rate is increased from 500 to 2,000 mA g^{-1}, the specific capacities of the $LiMn_2O_4$, $LiCr_{0.1}Mn_{1.9}O_4$ and $LiCr_{0.2}Mn_{1.8}O_4$ electrodes are decreased from 121.0, 116.4 and 105.4 to 89.6, 81.3 and 74.1 mAh g^{-1}, respectively, i.e., decreased by 26.0, 30.2 and 29.7%, respectively, indicating a good high-rate capability of the electrodes. Figure 6b shows the charge/discharge curves of the $LiCr_yMn_{2-y}O_4$ electrodes at the current rate of 500 mA g^{-1}. Two potential plateaus can be observed in the charge/discharge curves which correspond to the two couples of redox waves in the CVs. The discharge potentials and specific capacities of the electrodes follow the order of $LiMn_2O_4 > LiCr_{0.1}Mn_{1.9}O_4 > LiCr_{0.2}Mn_{1.8}O_4$, which are similar to the $LiCr_xMn_{2-x}O_4$ ($x = 0.00$–0.10) in a non-aqueous electrolyte [32].

The Li intercalation/deintercalation reaction of the $LiCr_yMn_{2-y}O_4$ electrode can be expressed as

$$LiCr_yMn_{2-y}O_4 \rightleftharpoons Li_{1-x}Cr_yMn_{2-y}O_4 + xLi^+ + xe^-$$

The theoretical specific capacity of a metal ion doped spinel $LiM_yMn_{2-y}O_4$ at the 4-V region depends on the mole fraction and oxidation number (oxidation state) of the doped metal ion and the amount of cation vacancy in the 16d site of $LiMn_2O_4$ [33]. Under the conditions of equal oxidation number and cation vacancy, the theoretical specific capacity should decrease with increasing the dopant content. Hence, in the present work, the specific capacity decreases with increasing the Cr content.

The cycle performances of the $LiCr_yMn_{2-y}O_4$ electrodes with different Cr contents at the high current rate of 2,000 mA g^{-1} over the operating potential range of 0–1.3 V (SCE) are displayed in Fig. 7. As can be seen, the capacity of the pristine $LiMn_2O_4$ electrode degrades fast in the initial 2,000 cycles. A stable capacity is maintained from ca. 2,000 to 3,500 cycles, but fades again after 3,500 cycles. After 5,000 cycles, 69% of the initial capacity is maintained. The initial specific capacity of the $LiCr_{0.1}Mn_{1.9}O_4$ electrode is lower than that of the pristine $LiMn_2O_4$ electrode. No capacity degradation could be observed in the initial 1,000 cycles, but it degrades from ca. 1,000th cycle. After 7,500 cycles, 70% of the initial capacity is maintained. The initial specific capacity of the $LiCr_{0.2}Mn_{1.8}O_4$ electrode is lower than those of the $LiMn_2O_4$ and $LiCr_{0.1}Mn_{1.9}O_4$ electrodes. However, its fading rate is the lowest. After 10,000 cycles, 73% of the initial capacity is maintained. In addition, as seen by the absolute values of specific capacity of the electrodes, the specific capacity of the $LiCr_{0.1}Mn_{1.9}O_4$ electrode exceeds that of the pristine $LiMn_2O_4$ electrode after ca. 300 cycles. The specific capacity of the $LiCr_{0.2}Mn_{1.8}O_4$

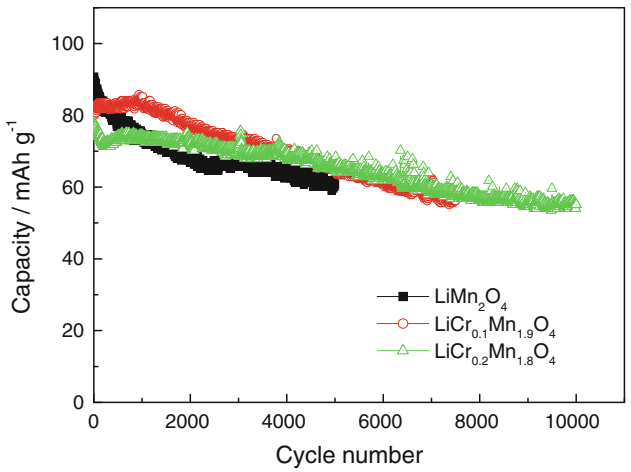

Fig. 7 Cycle performances of $LiCr_yMn_{2-y}O_4$ electrodes with different Cr contents at a high current rate of 2,000 mA g^{-1}

electrode exceeds that of the pristine $LiMn_2O_4$ electrode after ca. 1,000 cycles, and exceeds that of the $LiCr_{0.1}Mn_{1.9}O_4$ after ca. 4,300 cycles. Thus it can be seen that the cyclic stability of the electrodes follow the order of $LiCr_{0.2}Mn_{1.8}O_4 > LiCr_{0.1}Mn_{1.9}O_4 > LiMn_2O_4$. That is to say, the cyclic stability increases with increasing Cr content. Cr-doping can obviously improve the cyclic stability of $LiMn_2O_4$ in 5 M $LiNO_3$ solution in comparison with the pristine $LiMn_2O_4$. The improved cyclic stability by Cr-doping should be attributed to the depression of Jahn–Teller distortion [18] together with the stabilization of the octahedral sites by the stronger Cr–O bands in the delithiated state (comparing the binding energy of 1,142 kJ mol^{-1} for CrO_2 with 946 kJ mol^{-1} for α-MnO_2) [21]. The two factors would be responsible for the stabilization of the spinel structure of $LiMn_2O_4$.

4 Conclusions

In this paper, spinel $LiCr_yMn_{2-y}O_4$ ($y = 0$, 0.1, 0.2) electrode materials were prepared via a sol–gel method starting with lithium acetate, manganese acetate, chromium nitrate and citric acid raw materials. XRD results revealed that the synthesized $LiCr_yMn_{2-y}O_4$ materials take the cubic spinel structure. Cr-doping does not change the phase structure of the Cr-doped $LiMnO_4$. The $LiCr_yMn_{2-y}O_4$ materials show the morphology of aggregates composed of crystallites. The size of the crystallites increases with increasing calcination temperature, and the Cr-doped spinels show a wider crystallite size distribution, which are confirmed by TEM and SEM. Electrochemical result demonstrated that Cr-doping can markedly improve the high-rate charge/discharge cyclability of the $LiMnO_4$ electrode in 5 M $LiNO_3$ aqueous solution. 73% of the initial capacity is maintained after 10,000 charge/discharge cycles for the $LiCr_{0.2}Mn_{1.8}O_4$ electrode at a high current rate of 2,000 mA g^{-1}, which is obviously superior to that of the pristine $LiMn_2O_4$ electrode. The Cr-doped spinel $LiMnO_4$ would be a promising candidate material for use as positive electrodes in aqueous high-rate lithium ion batteries and electrochemical supercapacitors, especially for supercapacitors.

Acknowledgments This work was supported by Leading Academic Discipline Project of Shanghai Municipal Education Commission (Project Number: J50102). Center of Instrumental Analysis and Test of Shanghai University is gratefully acknowledged for XRD, SEM and TEM experiments.

References

1. Li W, Dahn JR, Wainwright DS (1994) Science 264:1115
2. Wang GX, Zhong S, Bradhurst DH, Dou SX, Liu HK (1998) J Power Sour 74:198
3. Luo JY, Xia YY (2007) Adv Funct Mater 17:3877
4. Wang GJ, Zhao NH, Yang LC, Wu YP, Wu HQ, Holze R (2007) Electrochim Acta 52:4911
5. Wang HB, Zeng YQ, Huang KL, Liu SQ, Chen LQ (2007) Electrochim Acta 52:5102
6. Liu XH, Saito T, Doi T, Okada S, Yamaki J (2009) J Power Sour 189:706
7. Li NC, Patrissi CJ, Che GL, Martin CR (2000) J Electrochem Soc 147:2044
8. Eftekhari A (2001) Electrochim Acta 47:495
9. Jayalakshmi M, Mohan Rao M, Scholz F (2003) Langmuir 19:8403
10. Lee JW, Su-Il P (2004) Electrochim Acta 49:753
11. Nakayama N, Nozawa T, Iriyama Y, Abe T, Ogumi Z, Kikuchi K (2007) J Power Sour 174:695
12. Cvjeticanin N, Stojkovic I, Mitric M, Mentus S (2007) J Power Sour 174:1117
13. Tonti D, Torralvo MJ, Enciso E, Sobrados I, Sanz J (2008) Chem Mater 20:4783
14. He P, Luo JY, He JX, Xia YY (2009) J Electrochem Soc 156:A209
15. Katakura K, Wada K, Kajiki Y, Yamamoto A, Ogumi Z (2009) J Power Sour 189:240
16. Chen SY, Mi CH, Su LH, Gao B, Fu QB, Zhang XG (2009) J Appl Electrochem 39:1943
17. Tian L, Yuan AB (2009) J Power Sour 192:693
18. Nieto S, Majumder SB, Katiyar RS (2004) J Power Sour 136:88
19. Kakuda T, Uematsu K, Toda K, Sato M (2007) J Power Sour 167:499
20. Liu RS, Shen CH (2003) Solid State Ion 157:95
21. Thirunakaran R, Kim KT, Kang YM, Seo CY, Young-Lee J (2004) J Power Sour 137:100
22. Wang XQ, Tanaike O, Kodama M, Hatori H (2007) J Power Sour 168:282
23. Hwang BJ, Tsai YW, Santhanam R, Hu SK, Sheu HS (2003) J Power Sour 119–121:727
24. Pascual L, Gadjov H, Kovacheva D, Petrov K, Herrero P, Amarilla JM, Rojas RM, Rojo JM (2005) J Electrochem Soc 152:A301
25. Hwang SJ, Park DH, Choy JH, Campet G (2004) J Phys Chem B 108:12713
26. Taniguchi I (2005) Ind Eng Chem Res 44:6560

27. Singh G, Panwar A, Sil A, Ghosh S (2009) Ceram Silik 53:260
28. Zhang D, Popov BN, White RE (1998) J Power Sour 76:81
29. Zeng RH, Li WS, Lu DS, Huang QM (2007) J Power Sour 174:592
30. de Levie R (1963) Electrochim Acta 8:751
31. Lu DS, Li WS, Zuo XX, Yuan ZZ, Huang QM (2007) J Phys Chem C 111:12067
32. Shen PZ, Huang YD, Liu L, Jia DZ, Guo ZP (2006) J Solid State Electrochem 10:929
33. Todorov YM, Hideshima Y, Noguchi H, Yoshio M (1999) J Power Sour 77:198